
Physics-Informed Neural Network Super Resolution for Advection-Diffusion Models

Chulin Wang; Eloisa Bentivegna; Wang Zhou; Levente J. Klein; Bruce Elmeegreen
IBM Research
{wangc,eloisa.bentivegna,wang.zhou}@ibm.com; {kleinl,bge}@us.ibm.com

Abstract

Physics-informed neural networks (NN) are an emerging technique to improve spatial resolution and enforce physical consistency of data from physics models or satellite observations. A super-resolution (SR) technique is explored to reconstruct high-resolution images (4x) from lower resolution images in an advection-diffusion model of atmospheric pollution plumes. SR performance is generally increased when the advection-diffusion equation constrains the NN in addition to conventional pixel-based constraints. The ability of SR techniques to also reconstruct missing data is investigated by randomly removing image pixels from the simulations and allowing the system to learn the content of missing data. Improvements in S/N of 11% are demonstrated when physics equations are included in SR with 40% pixel loss. Physics-informed NNs accurately reconstruct corrupted images and generate better results compared to the standard SR approaches.

1 Introduction

Modeling physical systems is often limited to coarse spatial and temporal grid resolution due to the exponential dependence of computing requirements on the grid sizes [1]. While traditional super resolution (SR) techniques [2, 3, 4, 5] can boost model granularity by minimizing pixel-level differences between high-resolution (HR) data and super-resolved output made from low resolution (LR) input, the output may not capture the physical, ecological or geological processes at work that are governed by physical laws. Besides, real observations like satellite images [6] are sparse and often incomplete, leading to “missing pixels.” How to fill in missing values while maintaining physical consistency remains an open question.

Here we propose a physics-informed neural network for SR (PINNSR) method that incorporates both traditional SR techniques and fundamental physics. In addition to minimizing pixel-wise differences, PINNSR also enforces the governing physics laws by minimizing a physics consistency loss. We apply PINNSR to plume simulations based on the advection-diffusion equation with variable wind conditions, which is considered as a proxy for remote satellite observations of pollutant gas dispersion [6]. Compared to traditional SR methods, our approach demonstrates that:

- Data from a first-principle advection-diffusion equation at low resolution can be forced to reconstruct physically meaningful data rather than the numerical interpolation of the LR data.
- The additional physics constraints increase the accuracy in reconstruction of HR data for both physics-governed processes and missing-value conditions.
- Physics consistency loss can quantify how reliably the SR generated data reproduce the physics laws.
- SR for physics-related data should be modeled from direct observations of LR and HR data, compared to synthetic LR from bicubic downsampling in typical computer vision problems.

2 Related Work

SR with neural networks (NN) has been extensively studied in recent years. SRCNN [2] firstly adopted a three-layer CNN to represent the mapping function. Deeper and wider networks [7, 8, 9, 10, 11] with residual learning were proposed to enhance the performance. SRGAN [3] adopted generative adversarial networks (GANs) [12] and showed better perceptual quality. EDSR [4] improved the generation by removing batch-normalization, and residual-in-residual blocks (RRDB) introduced by ESRGAN [5] further boosted the performance.

There has been growing interest in applying SR to physics-related data. Fukami *et al.* [13] used the SRCNN network structure to super-resolve 2D laminar cylinder flow. MeshfreeFlowNet [14] used a U-Net structure to reconstruct the Rayleigh-Bénard instability. PIESRGAN [15] utilized the ESRGAN architecture for turbulence modeling. In all of these models, the LR input was generated from down-sampling the HR dataset, so part of the NN learning could be the reverse of the down-sampling algorithm itself, making the models unpractical for data deviating from the same down-sampling process.

3 Method

3.1 Plume simulations

Common prior arts for SR use down-sampled HR images to approximate the LR input. This assumption limits the modeling to be the down-sampling kernel (normally bicubic interpolation). For example, unstable flows like the Rayleigh-Taylor instability, which grows fastest at the shortest wavelengths, have different growth rates and structures at different resolutions. Thus a naive bicubic interpolation cannot capture the mapping between LR and HR.

Here we simulate atmospheric dispersion of gaseous plumes through integration of the advection-diffusion equation for the gas concentration C in 2D:

$$\partial_t C + \nabla \cdot C \mathbf{u} = \nabla \cdot (\mathbf{K} \cdot \nabla C) + S, \quad (1)$$

where \mathbf{u} is the atmospheric velocity field, \mathbf{K} is the diffusivity tensor, and S is a source (or sink) term. In this work, LR and HR datasets are *both* generated by running the simulation model twice but at different spatial grid sizes for each of the random source placements, with the HR simulation having $4\times$ finer resolution than the LR simulation. Snapshots of the gas concentration $C^{(t)}$ are saved to construct LR-HR (input-output) training pairs. More details can be found in Appendix A.

3.2 PINNSR network

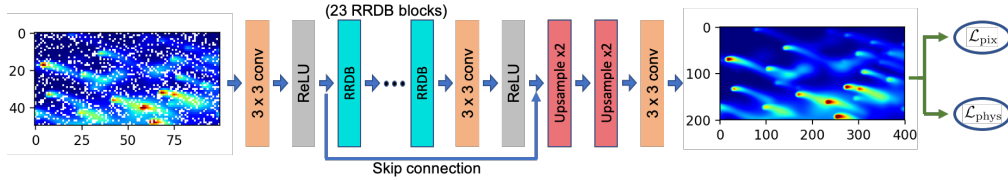


Figure 1: Network structure of PINNSR. The input LR is generated by simulating on a coarse grid instead of down-sampling from HR. Random pixels are dropped (shown in white) to imitate missing pixels. The total loss is a weighted sum of pixel loss \mathcal{L}_{pix} and physics consistency loss $\mathcal{L}_{\text{phys}}$.

The base network of PINNSR is built on multiple RRDB blocks [5], as shown in Figure 1. Whereas [5] employs a discriminator to improve the visual quality at a cost of reduced peak signal-to-noise ratio (PSNR), for physics-based data, it is preferred to have high PSNR. Thus, no discriminator is included for PINNSR. Instead, we introduce a *physics consistency loss*

$$\mathcal{L}_{\text{phys}} = \|R(C_{\text{SR}}) - R(C_{\text{HR}})\|_1, \quad (2)$$

which minimizes the physics residual $R(C)$ between SR and HR. The physics residual $R(C)$ is defined from the governing advection-diffusion equation:

$$R(C) = \partial_t C + \nabla \cdot C \mathbf{u} - \nabla \cdot (\mathbf{K} \cdot \nabla C) - S, \quad (3)$$

where the derivatives are calculated using a finite-difference approximation. Due to this approximation and the resulting truncation error, $R(C)$ is not zero but the sum of all the higher-order terms neglected when computed at the relevant resolution, and thus Equation 2 minimizes the difference in $R(C)$. A visualization of the HR image and each term of the corresponding physics residual is illustrated in Figure 2. As shown in panel (b), the residual is mostly 0 for the entire image, except near the “edge” of each source location and along the center of the plume where the truncation error is the highest.

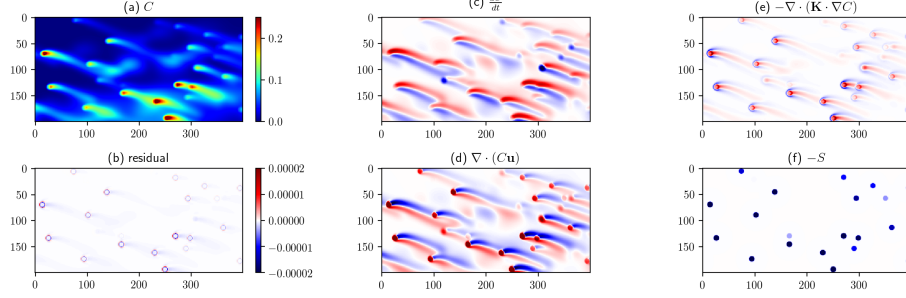


Figure 2: (a) The HR image for 20 randomly distributed plume sources under variable wind conditions; (b) Physics residual term $R(C)$ due to numerical rounding errors; (c) - (f) Different terms of advection-diffusion equation that contribute to the HR image.

As depicted in Figure 1, the total loss \mathcal{L}_{tot} is a weighted sum of the pixel loss \mathcal{L}_{pix} and the physics consistency loss $\mathcal{L}_{\text{phys}}$, with weighting parameter η and batch size N :

$$\begin{aligned}\mathcal{L}_{\text{tot}} &= \mathcal{L}_{\text{pix}} + \eta \cdot \mathcal{L}_{\text{phys}} \\ &= \frac{1}{N} \sum_{i=1}^N \|C_{\text{SR}} - C_{\text{HR}}\|_1 + \eta \cdot \frac{1}{N} \sum_{i=1}^N \|R(C_{\text{SR}}) - R(C_{\text{HR}})\|_1.\end{aligned}\quad (4)$$

4 Experiments

4.1 Dataset

As explained in Section 3.1, the dataset is constructed to simulate the atmospheric dispersion of gaseous plumes using Equation 1 for both LR and HR spatial scales. For each of the input-output pairs, snapshots of gas concentration are stacked as 3-channel images in the order of $C^{(t-1)}$, $C^{(t)}$, and $C^{(t+1)}$ to allow estimation of the time derivative. The spatial gradients and time derivatives for the physics equation are evaluated by first-order centered differences on the space-time grid.

To make the problem more physically relevant to real satellite data, some of the pixels in the LR images are randomly dropped to simulate cloud cover, non-convergent flux calculations, and other glitches. Experiments are conducted at various dropping rates (0%, 20%, 40%, and 60%) to study the robustness of the method.

4.2 Baselines and metrics

Bicubic. For a baseline model, we use bicubic interpolation to first fill the missing pixels (if there are any), and then the SR images are generated by a $4\times$ bicubic upsampling.

Downsampled HR (Dwn-HR). The network is trained with downsampled HR as input. This is commonly done for SR datasets [16, 17, 18, 5]. However, to mimic the real situation where LR is available but not HR, we test the trained model on *simulated* LR instead of downsampled HR.

Standard SR (Std-SR). The network is trained on simulated LR and HR pairs but without the physics consistency loss $\mathcal{L}_{\text{phys}}$.

PINNSR. Our proposed approach trains the network on simulated LR and HR pairs with a weighted sum of the pixel loss \mathcal{L}_{pix} and the physics consistency loss $\mathcal{L}_{\text{phys}}$.

Metrics. Models are evaluated by the standard PSNR and structural similarity (SSIM). In addition, we include the physics consistency loss $\mathcal{L}_{\text{phys}}$ as another metric to measure the fidelity on governing physics laws. Visual illustrations of the pixel differences are also presented.

4.3 Results

Table 1: Comparison of test results for different models (the best results are in bold).

Pixel drop	PSNR / 1 - SSIM / $\mathcal{L}_{\text{phys}}$			
	Bicubic	Dwn-HR	Std-SR	PINNSR
0%	45.73 / 0.0065 / 5.9E-7	45.85 / 0.0058 / 1.1E-6	82.29 / 2.1E-6 / 2.8E-7	82.83 / 2.0E-6 / 0.9E-7
20%	45.42 / 0.0070 / 6.4E-7	45.17 / 0.0064 / 1.5E-6	82.35 / 0.9E-6 / 1.8E-7	82.71 / 1.5E-6 / 1.2E-7
40%	44.79 / 0.0080 / 7.2E-7	44.83 / 0.0065 / 1.1E-6	81.19 / 1.5E-6 / 3.0E-7	82.12 / 1.3E-6 / 1.5E-7
60%	43.26 / 0.0128 / 8.8E-7	44.66 / 0.0061 / 0.8E-6	78.44 / 2.7E-6 / 4.1E-7	79.02 / 2.3E-7 / 2.6E-7

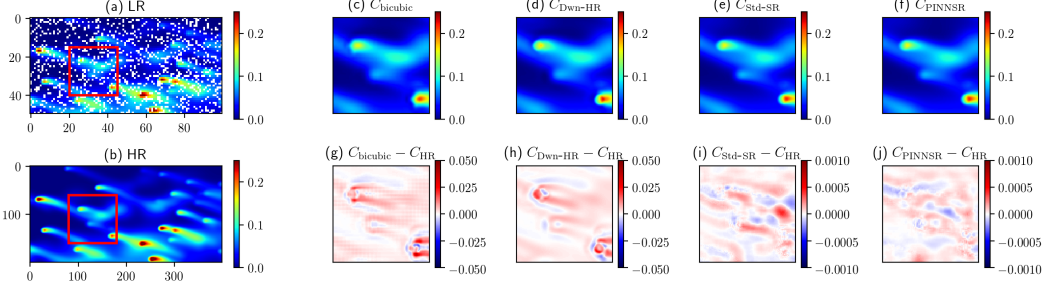


Figure 3: Qualitative comparison between different SR models from the test set when 20% of the pixels are dropped. (a) LR input; (b) ground truth HR output; (c) - (f) SR generated by bicubic, Dwn-HR, Std-SR, and PINNSR; (g) - (j) the corresponding pixel residual calculated from $C_{\text{SR}} - C_{\text{HR}}$, the PINNSR clearly out-performs other models. Additional visualizations can be found in Appendix C.

Table 1 summarizes our results. In all cases, PINNSR yields higher PSNR and better physics consistency, which confirms that the physics consistency loss introduced at training helps to regulate the learning and improve the performance. The additional physics information not only enforces the output to comply with physics laws better (lower $\mathcal{L}_{\text{phys}}$), but also improves the accuracy in generating SR output. As shown in Figure 3(j), the pixel difference of PINNSR is smaller than Std-SR and 2 orders of magnitude lower compared to Bicubic. The improvement is persistent for all pixel drop rates, and the case with 40% pixel drop has the best improvement with physics compared to Std-SR, increasing PSNR by 0.93 dB which corresponds to an 11% decrease in rms error.

Dwn-HR can achieve unusually high PSNR ~ 100 (Appendix D) when the training and testing are both conducted on downsampled HR as input. But the same model, when tested with simulated LR, performs poorly with PSNR ~ 45 , which is close to bicubic upsampling. Comparing Figure 3 (h) and (g), the patterns are very similar. This indicates that when trained with bicubically downsampled HR as input, Dwn-HR learns a reverse mapping (bicubic upsampling). When applied to data that differ from bicubic interpolation (like simulated LR), the performance of the model degrades significantly. Therefore, for physics-based data shown here, it is better to learn the mapping from LR to HR from direct observations of LR and HR rather than using downsampled HR with the assumption that the mapping can be captured by a known kernel (like bicubic interpolation).

To perform SR with missing pixels, an intuitive approach is to use bicubic interpolation to fill in the missing pixels first and then pass it to an SR model. We show that PINNSR learns the relations between existing and missing pixels and performs better than the two-step approach. More details are explained in Appendix E.

5 Conclusions

We proposed a PINNSR method for super resolution on advection-diffusion modeling and demonstrated superior performance on both reconstruction accuracy and physics consistency. This is done by introducing a physics consistency loss to regulate model training. The method is robust even if pixels are missing as commonly observed in satellite images. The method can be generalized to other physics problems governed by different physics laws.

Broader Impact

Multiple satellites are enabling remote observations of the Earth’s surface, even multiple times per day. Satellite images are affected by missing pixels and resolution that is spatially too coarse to identify greenhouse gas sources and polluters. Here we introduce a Physics-Informed Neural Network that creates physically consistent high-resolution imagery from low quality and low-resolution simulations based on an advection-diffusion equation. The reconstructed missing data follows the underlying physics law and demonstrates a robust way to ensure the physics consistency of the super-resolution imagery. Reconstructing missing data and increasing the spatial resolution of current satellite imagery, based on solid physics principles, can create trustworthy and verifiable data that increase transparency in identifying pollution sources.

References

- [1] Lawrence Buja Washington, Warren M. and Anthony Craig. The computational future for climate and earth system models: on the path to petaflop and beyond. *Philosophical Transactions of the Royal Society A: Mathematical, Physical and Engineering Sciences*, pages 833–846, 2009.
- [2] Chao Dong, Chen Change Loy, Kaiming He, and Xiaoou Tang. Learning a deep convolutional network for image super-resolution. In *European conference on computer vision*, pages 184–199. Springer, 2014.
- [3] Christian Ledig, Lucas Theis, Ferenc Huszar, Jose Caballero, Andrew Cunningham, Alejandro Acosta, Andrew Aitken, Alykhan Tejani, Johannes Totz, Zehan Wang, and Wenzhe Shi. Photo-realistic single image super-resolution using a generative adversarial network. *Proceedings of the IEEE conference on computer vision and pattern recognition*, 1:4681–4690, 2017.
- [4] Bee Lim, Sanghyun Son, Heewon Kim, Seungjun Nah, and Kyoung Mu Lee. Enhanced deep residual networks for single image super-resolution. In *Proceedings of the IEEE conference on computer vision and pattern recognition workshops*, pages 136–144, 2017.
- [5] Xintao Wang, Ke Yu, Shixiang Wu, Jinjin Gu, Yihao Liu, Chao Dong, Yu Qiao, and Chen Change Loy. Esrgan: Enhanced super-resolution generative adversarial networks. In *Proceedings of the European Conference on Computer Vision (ECCV)*, pages 0–0, 2018.
- [6] Oliver Schneising, Michael Buchwitz, Maximilian Reuter, Heinrich Bovensmann, John Burrows, Tobias Borsdorff, and Nicholas M. Deutscher. A scientific algorithm to simultaneously retrieve carbon monoxide and methane from tropomi onboard sentinel-5 precursor. *Atmospheric Measurement Techniques*, pages 6771–68802, 2019.
- [7] Jiwon Kim, Jung Kwon Lee, and Kyoung Mu Lee. Accurate image super-resolution using very deep convolutional networks. In *Proceedings of the IEEE conference on computer vision and pattern recognition*, pages 1646–1654, 2016.
- [8] Jiwon Kim, Jung Kwon Lee, and Kyoung Mu Lee. Deeply-recursive convolutional network for image super-resolution. In *Proceedings of the IEEE conference on computer vision and pattern recognition*, pages 1637–1645, 2016.
- [9] Tao Dai, Jianrui Cai, Yongbing Zhang, Shu-Tao Xia, and Lei Zhang. Second-order attention network for single image super-resolution. In *Proceedings of the IEEE conference on computer vision and pattern recognition*, pages 11065–11074, 2019.
- [10] Ying Tai, Jian Yang, and Xiaoming Liu. Image super-resolution via deep recursive residual network. In *Proceedings of the IEEE conference on computer vision and pattern recognition*, pages 3147–3155, 2017.
- [11] Ying Tai, Jian Yang, Xiaoming Liu, and Chunyan Xu. Memnet: A persistent memory network for image restoration. In *Proceedings of the International Conference on Computer Vision*, pages 4539–4547, 2017.

- [12] Ian Goodfellow, Jean Pouget-Abadie, Mehdi Mirza, Bing Xu, David Warde-Farley, Sherjil Ozair, Aaron Courville, and Yoshua Bengio. Generative adversarial nets. In *Advances in neural information processing systems*, pages 2672–2680, 2014.
- [13] Kai Fukami, Koji Fukagata, and Kunihiko Taira. Super-resolution reconstruction of turbulent flows with machine learning. *arXiv preprint arXiv:1811.11328*, 2018.
- [14] Chiyu Max Jiang, Soheil Esmaeilzadeh, Kamyar Azizzadenesheli, Karthik Kashinath, Mustafa Mustafa, Hamdi A Tchelepi, Philip Marcus, Anima Anandkumar, et al. Meshfreeflownet: A physics-constrained deep continuous space-time super-resolution framework. *arXiv preprint arXiv:2005.01463*, 2020.
- [15] Mathis Bode, Michael Gauding, Zeyu Lian, Dominik Denker, Marco Davidovic, Konstantin Kleinheinz, Jenia Jitsev, and Heinz Pitsch. Using physics-informed super-resolution generative adversarial networks for subgrid modeling in turbulent reactive flows. *arXiv preprint arXiv:1911.11380*, 2019.
- [16] Eirikur Agustsson and Radu Timofte. Ntire 2017 challenge on single image super-resolution: Dataset and study. In *Proceedings of the IEEE Conference on Computer Vision and Pattern Recognition Workshops*, pages 126–135, 2017.
- [17] Radu Timofte, Eirikur Agustsson, Luc Van Gool, Ming-Hsuan Yang, and Lei Zhang. Ntire 2017 challenge on single image super-resolution: Methods and results. In *Proceedings of the IEEE conference on computer vision and pattern recognition workshops*, pages 114–125, 2017.
- [18] Jia-Bin Huang, Abhishek Singh, and Narendra Ahuja. Single image super-resolution from transformed self-exemplars. In *Proceedings of the IEEE conference on computer vision and pattern recognition*, pages 5197–5206, 2015.
- [19] Frank Löffler, Joshua Faber, Eloisa Bentivegna, Tanja Bode, Peter Diener, Roland Haas, Ian Hinder, Bruno C. Mundim, Christian D. Ott, Erik Schnetter, Gabrielle Allen, Manuela Campanelli, and Pablo Laguna. The Einstein Toolkit: A Community Computational Infrastructure for Relativistic Astrophysics. *Class. Quant. Grav.*, 29:115001, 2012.
- [20] Sascha Husa, Ian Hinder, and Christiane Lechner. Kranc: a Mathematica package to generate numerical codes for tensorial evolution equations. *Computer Physics Communications*, 174:983–1004, 2006.
- [21] Erik Schnetter, Scott H. Hawley, and Ian Hawke. Evolutions in 3D numerical relativity using fixed mesh refinement. *Classical and Quantum Gravity*, 21(6):1465–1488, March 2004.

Appendices

A Simulation

To integrate the advection-diffusion equation (1), a numerical code is leveraged generated with the Cactus framework [19], using the automated code-generation package Kranc [20] and the Carpet mesh-refinement module [21]. A fourth-order finite differencing for spatial derivatives, and the Method of Lines technique (combined with fourth-order Runge-Kutta integration) is used to advance the solution in time. Periodic boundary conditions are applied to the outer boundaries.

In order to solve Equation (1) for gas concentration C , we first need to model the velocity \mathbf{u} and source S fields. S is modeled as a piece-wise constant function of compact spatial support (typically, as a function which is zero everywhere, except for a few scattered circles where S intermittently switches on and off).

In the advection-diffusion equation, the velocity field \mathbf{u} is assumed to be spatially constant with fluctuations in time around a given direction (i.e., the x direction):

$$\mathbf{u}(t) = \{u_0 + \sum_{i=1}^T u_i^x \cos(k_i^x t + \phi_i^x), \sum_{i=1}^T u_i^y \cos(k_i^y t + \phi_i^y)\} \quad u_i^x, u_i^y \ll u_0 \quad (5)$$

Figure 4 shows snapshots from a single-source plume model. Multiple-source profiles are obtained by superimposing several single-source solutions, centered at different points in the simulation domain. Since Equation (1) is linear in C and the wind velocity is spatially constant, the resulting superposition satisfies Equation (1) if so do the single-source components.

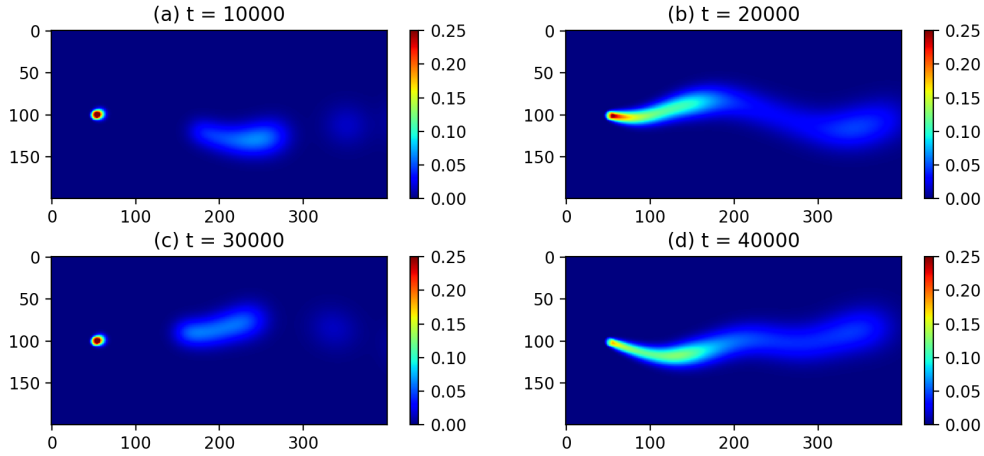


Figure 4: Snapshots from the evolution of a single plume model at different iteration steps.

B Training details

The LR simulations are of size 100×50 and HR simulations are of size 400×200 . Since the simulation model is expressed by a linear differential equation, an arbitrary superposition of the concentration map also satisfies the physics model. Moreover, the periodicity in wind velocity makes it possible to align concentration at different iteration steps as long as they differ by an integer number of periods. In particular, each training image has 20 plume sources randomly placed within the frame. The source flux is randomly sampled from a uniform distribution between 0 and maximum flux. Datasets are stored as 2D images with floating-point format ranging between 0 and 1. In total there are 2000 images with different random source placements, intensities, and start times.

At each training step, 16×16 LR patches are used as input and the corresponding HR patch size is 64×64 . For all the experiments we empirically set the weight $\eta = 100.0$ to balance the ratio

between the physics consistency loss and the pixel loss. A Cosine Annealing learning rate scheduler with restarts is used, adjusting the learning rate to decay from 2×10^{-4} to 1×10^{-7} within 2.5×10^5 iterations, and the whole process repeats 4 times. Adam optimizer with $\beta_1 = 0.9$ and $\beta_2 = 0.999$ is used for optimization. The model is implemented in PyTorch.

C Additional results

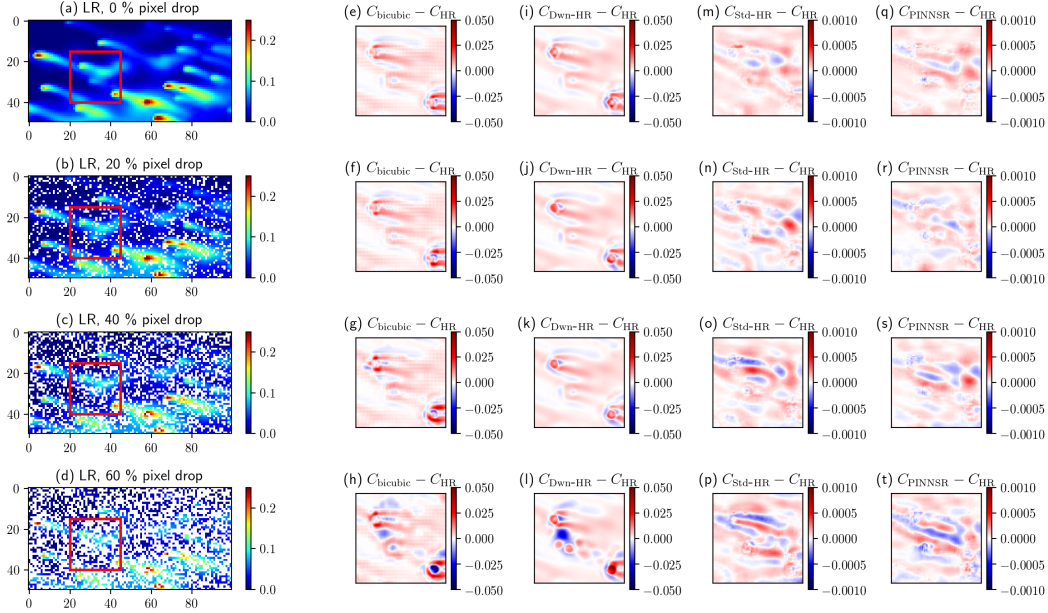


Figure 5: Qualitative comparison between different SR models for all pixel dropping rates. (a) - (d) LR input for 0% to 60% pixel drop rate; (e) - (h) SR generated by bicubic; (i) - (l) SR generated by Dwn-HR; (m) - (p) SR generated by Std-SR; (q) - (t) SR generated by PINNSR. Each row has the same pixel drop percentage.

For four scenarios where 0%, 20%, 40% and 60% of the pixels are dropped, the visual results are shown in Figure 5. Firstly, a higher missing pixel percentage corresponds to a larger pixel loss, and thus lowers PSNR. Secondly, within the same pixel drop percentage, $\text{PINNSR} < \text{Std-SR} \ll \text{bicubic} \approx \text{Dwn-HR}$ in terms of pixel error. This is also consistent with the results reported in Table 1.

D Down-sampled HR vs. native LR input

Traditionally, the input of the SR NN is generated by down-sampling the HR. However, in this work, we emphasize using native LR simulation as input. Here we demonstrate that down-sampled HR as input is an oversimplification of the problem.

Following the traditional process, let's consider the NN trained with down-sampled HR as input. The results are shown in Table 2. When the NN is also tested with down-sampled HR as input, it would result in PSNR as high as ~ 100 . However, this does not reflect the actual performance. At test time, the HR ground truth is not available, only native LR is available as input. As shown in column 2 of Table 2, the PSNR is ~ 45 , which is only on par with the performance of the bicubic baseline.

E Bicubic interpolation for missing pixel reconstruction

It is also possible to leverage bicubic interpolation to reconstruct missing pixels, and subsequently use the 0% pixel drop PINNSR model for upsampling. The results are summarized in Table 3. Recovering missing pixels using bicubic interpolation is slightly better than the bicubic baseline, but it does not have comparable performance to the models directly trained with missing pixel LR (Table 1).

Table 2: Evaluation for models trained with down-sampled HR as LR input. All models have poor performance on reconstructing native LR.

Pixel drop	PSNR / 1 - SSIM / $\mathcal{L}_{\text{phys}}$	
	Test with down-sampled HR as input	Test with native LR as input
0%	100.49 / 0.0 / 6.4E-8	45.85 / 0.0058 / 1.1E-6
20%	98.03 / 6E-8 / 6.6E-8	45.17 / 0.0064 / 1.5E-6
40%	98.69 / 6E-8 / 7.0E-8	44.83 / 0.0065 / 1.1E-6
60%	98.49 / 0.0 / 13.1E-8	44.66 / 0.0061 / 0.8E-6

Table 3: Evaluation for bicubic interpolation as a preprocessing step with 0% missing pixel NN model. The performance is not comparable to the models trained with missing pixels.

Pixel drop	PSNR / 1 - SSIM / $\mathcal{L}_{\text{phys}}$	
	Std-SR (0 %)	PINNSR (0 %)
0%	82.29 / 2.1E-6 / 2.8E-7	82.83 / 2.0E-6 / 0.9E-7
20%	56.68 / 6.8E-4 / 3.6E-6	57.16 / 6.6E-4 / 2.9E-8
40%	51.67 / 0.0025 / 4.4E-6	51.84 / 0.0024 / 3.8E-6
60%	46.90 / 0.0076 / 2.7E-6	46.92 / 0.0080 / 2.7E-6